Nonadiabatic molecular dynamics simulations of the photofragmentation and geminate recombination dynamics in size-selected $I_2^- \cdot Ar_n$ cluster ions

V. S. Batista[a] and D. F. Coker
Department of Chemistry, Boston University, 590 Commonwealth Avenue, Boston, Massachusetts 02215

(Received 12 December 1996; accepted 29 January 1997)

We investigate the photodissociation, geminate recombination and relaxation dynamics in size-selected $I_2^- \cdot Ar_n$ cluster ions using a coupled quantum-classical molecular dynamics method and a model Hamiltonian gained from diatomics-in-ionic systems. We calculate photofragmentation yields of various charged product clusters of the dissociated $I^- \cdot Ar_f$ or recombined $I_2^- \cdot Ar_{f'}$ forms as a function of precursor cluster size and find almost quantitative agreement with experimental results. The trends in photofragmentation are explained in terms of various participating electronically nonadiabatic channels coupled with vibrational relaxation on these different surfaces. We also explore the role of long range electrostatic interactions and underlying precursor cluster geometry on the photofragmentation dynamics. © *1997 American Institute of Physics.* [S0021-9606(97)03917-2]

I. INTRODUCTION

Studies of photofragmentation of simple solute chromophores in molecular clusters can in principle provide an understanding of the most elementary dynamical excited state chemical processes in the simplest model of condensed phase solvation conditions which can be probed in microscopic detail with experimental methods. These limited size systems are also ideally suited to detailed investigation using new advanced theoretical and computational methods for treating electronically excited state chemical reaction dynamics. This paper thus reports the first application of these new simulation methods[1–6] to the study of photoexcited reactions in cluster systems which have been probed in microscopic detail in recent experiments.

In recent years, several groups have applied ultrafast spectroscopic techniques to investigate cluster fragmentation,[7–10] the competition between fragmentation and ionization,[11,12] and photoinitiated chemical reactions in clusters.[7,11,13–19] The more recent experiments involve the use of both photofragmentation[20,21] and ultrafast pump-probe techniques[22,23] and have been applied to investigate the X_2^- (X=I,Br) photodissociation and cage recombination dynamics in size selected $X_2^- \cdot S_n$ (S=Ar,CO_2) ionic molecular clusters.[20,24,25]

I_2^- exhibits a strong absorption spectrum corresponding to an electronic excitation from the bound X, $^2\Sigma_{u,1/2}^+$ ground state to the repulsive A', $^2\Pi_{g,1/2}$ excited state[26] (see Fig. 3). In the gas phase, photoexcitation of this transition at 720–790 nm produces recoiling I and I^- photofragments with a kinetic energy release of $\sim$0.5 eV.[27] Due to this large amount of excess energy and the repulsive nature of the excited state potential one might think that a single, partially complete solvation shell expected with small molecular clusters of 10–20 atoms would be ineffective at caging the photofragments and inducing recombination. However, photoexcitation experiments on I_2^- in clusters of even fairly weakly interacting CO_2 molecules have detected coherent relaxation of I_2^- to the ground electronic state within a few picoseconds.[27] This relaxation time scale is strongly cluster size dependent and quite different from the vibrational relaxation timescales of the corresponding neutral species in liquids that are usually about two orders of magnitude longer.[28]

The subject of this article is thus to explore how excited state electrostatic solute/solvent interactions cause the nascent photofragments to be spatially trapped or ''caged.'' To this end we will develop an understanding of the electronically nonadiabatic processes which cause these caged photofragments to geminately recombine producing vibrationally excited starting material. Subsequent vibrational relaxation of these recombined molecular clusters deposits excess vibrational energy into the surroundings producing partial or total evaporation of solvent atoms from the cluster.

This sequential process of photodissociation, geminate recombination and vibrational relaxation has also been examined for I_2^- in liquids[29–34] as well as in a wide range of other systems, including both diatomic molecules and more complicated polyatomic systems. The most widely investigated of all such systems is the photodissociation and geminate recombination of I_2 in the condensed phase, for which solute/solvent interactions are dominated by the short range repulsive part of the potential. In recent work[6,35] we showed how semiempirical diatomics-in-molecules (DIM) electronic structure techniques could be implemented for giving a reliable description of the potential energy surfaces (PESs) involved in the process of relaxation and how to combine them with nonadiabatic molecular dynamics (MD) methods to provide a detailed description of the dynamics of photodissociation and geminate recombination of I_2 in liquids and solids.

In our DIM Hamiltonian model the solvent interactions that caused caging and recombination of the neutral I_2 were

[a]Present address: Department of Chemistry, University of California, Berkeley, CA 94720.

 0021-9606/97/106(17)/7102/15/$10.00

primarily short-range, collisional and repulsive in nature. At high solvent densities recombination was thus achieved with only a few collisions between the recoiling photofragments and the solvent. Thus, electrostatic solute/solvent interactions were not important in the relaxation processes. That system, however, provided an excellent test of our nonadiabatic molecular dynamics techniques since there are detailed experimental studies of the real time dynamics for both the gas and condensed phase systems.[28,36–40]

In this paper, we extend our semiempirical electronic structure calculations of PESs and the couplings among them to address the role of electrostatic interactions on condensed phase reaction dynamics. We report nonadiabatic MD simulations of the photofragmentation dynamics and geminate recombination in size selected $I_2^- \cdot Ar_n$ ionic molecular clusters and compare our results with recent photofragmentation experiments by Vorsa *et al.*[25] In these experimental studies the individual parent clusters were excited at specific laser frequencies and the caging fraction and the average loss of solvent molecules as function of cluster size and excitation energy were determined. We explore the effectiveness of the Ar solvent to cage photodissociated I_2^- and induce recombination of the chromophore through different reaction pathways, and explore the details of energy flow between the solvent and the solute as a function of cluster size. The role of many-body long range interactions in nonadiabatic dynamics that might be of primary importance for many other reactions in solution where strong electrostatic interactions between the solvent and an ionic solute might dominate the dynamics of the reaction are also studied.

Comparison between previous theoretical studies and experiments is uncertain since simulations were restricted to vibrational relaxation on the ground state,[41,42] whereas the experimental results depend on both electronic and vibrational relaxation. Furthermore, the only study to have treated the distortion effects in an entirely self-consistent manner approximated the solvent by a continuum model.[42] Other MD calculations have modeled the recombination dynamics of Br_2^- in clusters of argon and CO_2 using pairwise additive potentials and a variable charge method for modeling localization of the excess charge on one of the bromine atoms at large internuclear separations.[43–45] A one-hole model has been devised to treat the interaction of the six lowest electronic states of I_2^- with an arbitrary charge distribution and has been used to investigate mechanisms for nonadiabatic relaxation of electronically excited I_2^- in a CO_2 cluster, with the effects of the CO_2 molecules approximated by a uniform electric field parallel to the molecular axis of I_2^-.[42]

Reliable calculations face the difficulty of modeling the system of open-shell species undergoing excited state nonadiabatic dynamics with highly anisotropic many-body long range interaction potentials that have significant spin-orbit coupling contributions. In this paper we simulate the nonadiabatic dynamics of electronically excited I_2^- open-shell species using surface hopping nonadiabatic MD methods[1–6] with a model Hamiltonian gained from diatomics in ionic systems (DIIS) where we explicitly model the anisotropic and self consistent many-body nature of the interactions and include spin-orbit couplings using the proper PES for the I_2^- diatomic fragment.

The paper is organized as follows. In Sec. II A we first outline our approach to modelling the photoexcitation of the $I_2^- \cdot Ar_i$ cluster systems. Next, in Sec. II B, we summarize the method we employ for obtaining initial minimim energy structures and the equilibrium properties of size selected precursor clusters. Section II C outlines our calculation of the model Hamiltonian for these ionic molecular clusters, and Sec. II D describes our approximate computation of quantities necessary for the propagation of the nonadiabatic MD equations of motion. A summary of experimental observations is given in Sec. III A and a detailed comparison between the results of our calculations and the experimental findings is presented in Sec. III B. The paper is concluded in Sec. IV.

II. METHODS

A. Simulation of photofragmentation experiments

The approach we employ for simulating photofragmentation experiments involves first generating equilibrium configurations of the ground state $I_2^- \cdot Ar_i$ ionic molecular clusters for which the experimental pump frequencies are resonant with the energy difference between the ground X state and the A' state. Ensembles of 18 trajectories are first equilibrated for about 10 ps at 40 K and each individual trajectory is started from the undistorted minimum energy structure obtained according to the method described in Sec. II B. Each of these ground state equilibrated trajectories is then evolved adiabatically in the X state until the pump resonance condition at 790 nm is achieved. These pump resonant configurations are used as independent initial conditions for vertical photoexcitation to the A' state leaving all coordinates and velocities unchanged. The electronic expansion coefficient vectors are set to the appropriate initial unit vectors for the relevant photoexcitation in each ensemble member and nonadiabatic MD methods coupled with the semiempirical DIIS excited state electronic structure techniques presented later in Sec. II C are used to evolve the photoexcited ensemble of surface hopping trajectories in a manner consistent with the coherent propagated dynamical mixed state electronic wave function for each trajectory. We follow these nonadiabatic trajectories for 45 ps after photoexcitation. Experimental studies on cluster systems have revealed that electronic relaxation takes place in a few picoseconds and as we shall see this electronic relaxation is strongly coupled to cluster evaporation so trajectories of 45 ps duration should be long enough to see much of the expected cluster relaxation dynamics. We shall discuss longer time relaxation phenomena which these short trajectories cannot address later when we compare our results with experiment.

B. Minimum energy structures and equilibrium properties

Minimum energy structures are obtained with a classical MD simulation scheme analogous to other methods investi-

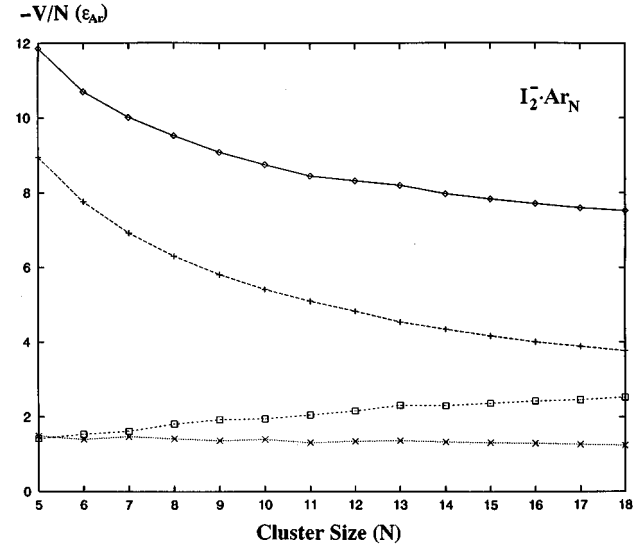

FIG. 1. Contributions to potential energy of minimum energy structures of $I_2^- \cdot Ar_n$ ($5 \leqslant n \leqslant 18$) clusters. Energy per Ar expressed in units of ϵ_{Ar} (83.26 cm^{-1}): total energy (diamonds), electrostatic polarization energy (+), Ar−Ar interaction energy (squares), and Ar−I interaction energy (×).

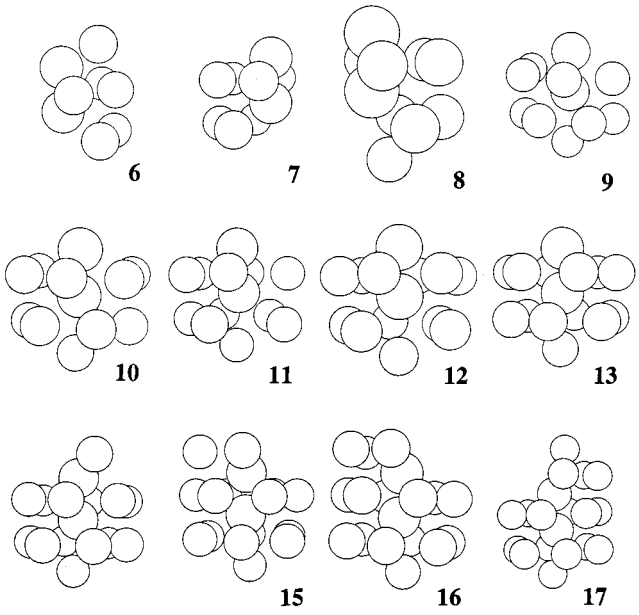

FIG. 2. Minimum energy structures of $I_2^- \cdot Ar_n$, $6 \leqslant n \leqslant 17$, the two larger diameter atoms embedded in the cluster are the I_2^- molecule.

gated in previous studies of equilibrium properties of similar cluster systems.[20,43–45] Initial configurations are chosen after the system is equlibrated at 150 K for more than 20 ps. At this initial temperature the system can not be trapped in an unfavorable structure because the rms bond fluctuations exceed ~0.1 Å, which is the usual criterion for cluster melting.[46]

Complete annealing of this randomly chosen configuration requires the use of several ''thermalization/equilibration/quenching'' cycles, where the thermalization and equilibration phases are performed at 50 K. The equations of motion for advancing the positions and velocities in the quenching phase of the dynamics are taken to be

$$m\ddot{\mathbf{r}} = \mathbf{F} - \gamma\dot{\mathbf{r}}, \tag{2.1}$$

where **F** are the forces in the ground state calculated according to Eq. (2.25) from the DIIS eigenvectors. These equations of motion (Eq. (2.1)) are integrated using the following results:

$$\mathbf{r}_{n+1} = \mathbf{r}_n + \dot{\mathbf{r}}_n h + [\mathbf{F}_n - \gamma\dot{\mathbf{r}}_n]\frac{h^2}{2m}, \tag{2.2}$$

$$\dot{\mathbf{r}}_{n+1} = \dot{\mathbf{r}}_n + [\mathbf{F}_n - \gamma\dot{\mathbf{r}}_n]\frac{h}{m}, \tag{2.3}$$

where we use a value for the friction constant $\gamma = 9$ a.u., and the integration time step is $h = 2.5$ fs. We use an ensemble of randomly sampled initial geometries to start these optimization runs and typically about 30% of these initial trajectories find the global minimum after just a few iterations of the above proceedure.

Figure 1 presents the energies of the lowest minimum energy structures expressed as energy divided by number of solvent particles. The most significant feature in this plot is that the total potential energy is dominated by the negative electrostatic contribution which is the sum of the charge-induced dipole, and induced dipole-induced dipole interactions. This electrostatic term gets smaller per particle as the cluster size is increased due to the competition between the negative charge-induced dipole interactions and the positive induced dipole-induced dipole interactions. Also these terms separately get smaller per particle with increasing cluster size since the dipoles induced in atoms added to the cluster which are further from the solvated charge are smaller.

Generally the short range interactions are not as important as the above long range electrostatic terms and they follow completely different trends. The short range Ar–I interactions in these equilibrium ground state configurations give an almost constant contribution per particle while the Ar–Ar Lennard-Jones interactions become slightly more negative with increasing cluster size as a result of increasing coordination numbers of the solvent atoms as these small clusters grow toward bulk coordination conditions. The relative magnitudes of the electrostatic and short range interactions we find here show the similar trends with cluster size to those reported by Amar and Perera who use a very different model to explore related molecular anion cluster systems.[43,44]

Minimum energy structures of the various size argon clusters solvating the I_2^- anion obtained using the optimization methods described above for the ground state potential surfaces calculated using the DIIS methods outlined in the following subsection are presented in Fig. 2. The underlying equilibrium structure of the I_2^- solvation shell in these small to intermediate size argon clusters is best understood in terms of forming a cylindrical stack of staggered hexagonal rings of argon atoms around the I_2^- anion. The first ring packs around the center of the I_2^- bond and subsequent rings

TABLE I. Molecular orbitals of I_2^-.

Case c type	Case c type wave function	Case a or b or $\Omega - s$ type	k_A	k_R	k_B	$EA_I + E_I^*$ (eV)
$X, \frac{1}{2u}$	$1/\sqrt{2}\{\|\frac{3}{2}-\frac{1}{2}\rangle\|S\rangle + \|S\rangle\|\frac{3}{2}-\frac{1}{2}\rangle\}$ $1/\sqrt{2}\{\|\frac{31}{22}\rangle\|S\rangle + \|S\rangle\|\frac{31}{22}\rangle\}$	$^2\Sigma^+_{u,1/2}$	1.32	2.52	0.63	3.06
$A, \frac{3}{2g}$	$1/\sqrt{2}\{\|\frac{3}{2}-\frac{3}{2}\rangle\|S\rangle - \|S\rangle\|\frac{3}{2}-\frac{3}{2}\rangle\}$ $1/\sqrt{2}\{\|\frac{33}{22}\rangle\|S\rangle - \|S\rangle\|\frac{33}{22}\rangle\}$	$^2\Pi_{g,3/2}$	0.30	1.30	0.73	3.06
$A', \frac{1}{2g}$	$1/\sqrt{2}\{\|\frac{3}{2}-\frac{1}{2}\rangle\|S\rangle - \|S\rangle\|\frac{3}{2}-\frac{1}{2}\rangle\}$ $1/\sqrt{2}\{\|\frac{31}{22}\rangle\|S\rangle - \|S\rangle\|\frac{31}{22}\rangle\}$	$^2\Pi_{g,1/2}$	0.10	1.82	0.73	3.06
$a, \frac{3}{2u}$	$1/\sqrt{2}\{\|\frac{3}{2}-\frac{3}{2}\rangle\|S\rangle + \|S\rangle\|\frac{3}{2}-\frac{3}{2}\rangle\}$ $1/\sqrt{2}\{\|\frac{33}{22}\rangle\|S\rangle + \|S\rangle\|\frac{33}{22}\rangle\}$	$^2\Pi_{u,3/2}$	(1.0×10^{-5})	2.80	0.69	3.06
$a', \frac{1}{2u}$	$1/\sqrt{2}\{\|\frac{11}{22}\rangle\|S\rangle + \|S\rangle\|\frac{11}{22}\rangle\}$ $1/\sqrt{2}\{\|\frac{1}{2}-\frac{1}{2}\rangle\|S\rangle + \|S\rangle\|\frac{1}{2}-\frac{1}{2}\rangle\}$	$^2\Pi_{u,1/2}$	(1.0×10^{-5})	3.30	0.9	2.12
$B, \frac{1}{2g}$	$1/\sqrt{2}\{\|\frac{11}{22}\rangle\|S\rangle - \|S\rangle\|\frac{11}{22}\rangle\}$ $1/\sqrt{2}\{\|\frac{1}{2}-\frac{1}{2}\rangle\|S\rangle - \|S\rangle\|\frac{1}{2}-\frac{1}{2}\rangle\}$	$^2\Sigma^+_{g,1/2}$	(1.0×10^{-5})	4.45	0.9	2.12

pack around the ends of the I_2^- molecule. Finally individual argon atoms pack onto the ends of the molecule, capping the end rings. The $i=13$ atom cluster shows a completed central ring and a single completed capped end structure. From Fig. 1 we see that this $i=13$ cluster is slightly more stable than its neighboring clusters since the completed rings optimize the Ar–Ar van der Waals interactions. As we move to larger clusters we see the second capping structure around the other end of the molecule being established. For smaller clusters we see competition between the formation of an incomplete central ring and a partial terminal cap structure.

C. Model Hamiltonian for $I_2^- \cdot Ar_n$

In this subsection we present the calculation of all polyatomic electronic states participating in the dynamics of relaxation and the couplings among the different surfaces that determine the rate of nonradiative electronic transitions. We implement the DIIS method where the polyatomic Hamiltonian is written as a sum of a DIM Hamiltonian and a perturbation term that introduces the induction energy which accounts for the self-consistent many-body nature of the electric field responsible for polarization. This method has been successfully investigated in studies of halogen atoms embedded in rare gas clusters[47,48] and in our recent calculations of ion-pair states of I_2 in rare gas matrices.[35]

We expand the time dependent electronic wave function of the polyatomic system, $\Psi(t)$, in terms of a canonical set of valence bond (VB) adiabatic state wave functions, $\phi_k(t)$,

$$\Psi(t)=\sum_k a_k(t)\phi_k(t), \tag{2.4}$$

and we write the VB wave functions, $\phi_k(t)$, in terms of diabatic polyatomic basis functions (pbf's), Φ_j,

$$\phi_k(t)=\sum_j \Gamma_{kj}\Phi_j, \tag{2.5}$$

where the expansion coefficients, Γ_{kj}, are the DIM eigenvectors. The pbf's, written as linear combinations of simple products of atomic functions (spaf's), are products of atomic and diatomic functions and are assumed to be eigenfunctions of their respective atomic and diatomic Hamiltonians with eigenvalues equal to experimental energies. The argon atoms and I^- ions are restricted to be in their ground states and we represent them by single $^1S_0$ functions since they have S symmetry closed shells. The I atoms have P-symmetry open shells and are represented with ^2P functions.

The diabatic polyatomic basis functions, Φ_j, are written as antisymmetrized products of S-symmetrical functions of the N argon atoms and $\zeta^{(j)}$ group functions of the iodide molecule,

$$\Phi_j=\hat{A}\zeta^{(j)}\prod_{i=1}^{N}|s^{(i)}\rangle, \tag{2.6}$$

where the index j indicates the electronic state of I_2^-. The zero overlap of atomic orbitals approximation (ZOAO), allows us to omit the antisymmetrization operator, $\hat{A}$, rendering the polyatomic wave function as a simple product of atomic and diatomic group functions. The error arising from this approximation is proportional to the square of the overlap integrals and has been shown to be small in DIM calculations on halogen atoms in nobel gases.[48]

Our basis set for the isolated I_2^- iodide molecule includes the six low-lying Hund's case (c) molecular states,

$$\zeta^{(j)}=(X_{1/2,u}, A_{3/2,g}, A'_{1/2,g}, a_{3/2,u}, a'_{1/2,u}, B_{1/2,g}),$$

arising from the $I^-(^1S_0)+I(^2P_{3/2,1/2})$ configurations. These states are presented in Table I distributed in two blocks according to their different dissociation limits, and these gas

phase curves are displayed in Fig. 3. They are classified among different symmetry species not only according to case (c) type classification but also according to case (a), (b) or $\Omega-s$ type. The latter has a well defined meaning only for fairly small internuclear separations, R, while the case (c) classification is applicable for large R values and is important for dissociation product correlations. In the first column of Table I we identify electronic states according to the value of the projection of the total angular momentum in the direction of the bond, $\Omega=|M^{(a)}+M^{(b)}|$. In the second column of the table we summarize expressions for the diatomic wave functions, $\zeta^{(j)}$. Any of these functions may be expressed by the linear combination

$$\zeta^{(j)}=c_1|J_j^{(a)}M_j^{(a)}\rangle|S^{(b)}\rangle+c_2|S^{(a)}\rangle|J_j^{(b)}M_j^{(b)}\rangle, \tag{2.7}$$

which is written in the basis set of spaf's, $\chi_{m,n}$, defined as

$$\begin{aligned}&\chi_{m,n}=|S\rangle|J^{(n)}M^{(n)}\rangle,\\ &J^{(n)}=3/2,1/2,\\ &M^{(n)}=-J^{(n)},-J^{(n)}+1,\ldots,J^{(n)},\end{aligned} \tag{2.8}$$

where m enumerates the different $|J^{(n)}M^{(n)}\rangle$ states of I atom n in the total angular momentum representation (coupled representation), $\mathbf{J}=\mathbf{L}+\mathbf{S}$ and M is the projection of $\mathbf{J}$ in the direction of the bond. States with Ω different from zero are double degenerate. Each degenerate state corresponds to one of the two possible orientations for the projection of the total angular momentum in the direction of the bond. Consequently the 6 Hund's case (c) molecular states form a basis set of 12 states including degeneracies.

The energy levels of the system are obtained now in the usual way by forming the Hamiltonian matrix of order 12×12.

Due to the lack of interatomic (atomic-diatomic) electron permutations in the polyatomic functions (ZOAO version of Eq. (2.6)), the Hamiltonian of the system can be partitioned into interatomic and atomic terms according to[49]

$$\hat{H}=\sum_K\sum_{L>K}H^{(KL)}-n\sum_K H^{(K)}, \tag{2.9}$$

where $H^{(K)}$ is the Hamiltonian operator of atom K and contains all kinetic energy operators and intraatomic potential energy terms that depend solely on the position of atom K and on the coordinates of those electrons initially assigned to this atom. Similarly, $H^{(KL)}$ is the Hamiltonian operator appropriate for the diatomic fragment KL.

The diatomic fragment Hamiltonian for I_2^- is constructed from potential energy curves for states listed in Table I, which are presented in Fig 3 and approximated by gas phase Morse functions[50]

$$\begin{aligned}V_{I_2^-}=D_{I_2^-}[&-2e^{(-\beta_{I_2^-}(R-R_{e,I_2^-}))}\\&+e^{(-2\beta_{I_2^-}(R-R_{e,I_2^-}))}]-(EA_I+E_I^*),\end{aligned} \tag{2.10}$$

where parameters k_A, k_B, k_R and $EA_I+E_I^*$ are presented in columns 4–7 of Table I. E_I^* is the energy of the particular excited state of I relative to the ground state, EA_I is the electron affinity of I and the relationships between the negative ion properties and the neutral properties are as follows:[51,50]

$$D_{I_2^-}=D_{I_2}\left(\frac{k_A}{k_B}\right), \tag{2.11}$$

where $D_{I_2}=1.58$ eV is the spectroscopic bond dissociation energy of the neutral I_2 molecule,

$$R_{e,I_2^-}=\frac{\ln(k_B/k_A)}{k_B\beta_{I_2}}+R_{e,I_2}, \tag{2.12}$$

where Morse parameters for the neutral I_2 molecule are $\beta_{I_2}=1.84$ Å^{-1} and $R_{e,I_2}=2.67$ Å, and

$$\beta_{I_2^-}=k_B\beta_{I_2}. \tag{2.13}$$

These DIM basis states are taken as a diabatic basis and we assume that intramolecular coupling of states with the same symmetry is small compared to intermolecular coupling introduced by the solvent.

The $H^{I^{(j)}Ar^{(i)}}$ Hamiltonian is written in the reference frame of the diatomic fragment $I^{(j)}Ar^{(i)}$ in terms of Ar–I potentials of the usual Σ, Π and $\overline{\Pi}$ orientations as described in Ref. 52. These potentials are constructed using the MMSV (Morse–Morse-switching function–van der Waals) potential forms from Ref. 53 for the X 1/2, I 3/2 and II 1/2 potentials. The X 1/2 and I 3/2 states correlate with the $^2P_{3/2}+{}^1S_0$ asymptote, while the II 1/2 correlates with $^2P_{1/2}+{}^1S_0$. 1/2 and 3/2 following X, I, and II are the Ω quantum numbers where Ω is the projection of the total electronic angular momentum along the molecular axis. In this paper we follow the convention presented in our previous papers[6,35] where vector Σ is in the reference frame of the diatomic fragment oriented along the $\mathbf{R}_{ij}$ vector, Π is perpendicular to Σ and located in the plane formed by $\mathbf{R}_{ij}$ and the x axis while $\overline{\Pi}$ is perpen-

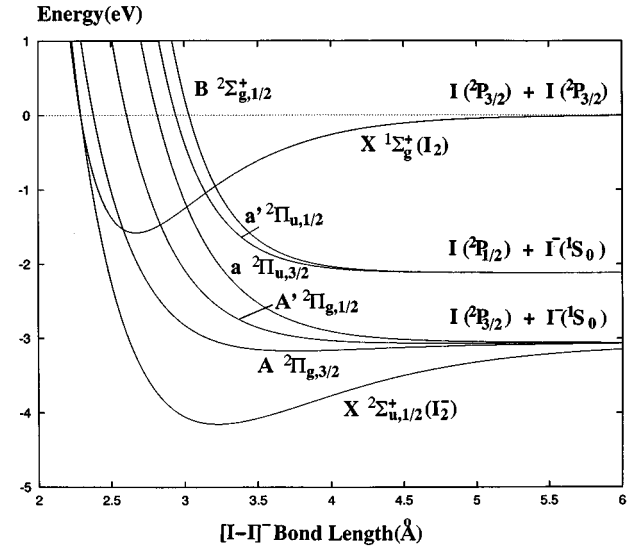

FIG. 3. Gas phase I_2^- potential energy surfaces calculated as described. The ground state for the neutral I_2 species is also shown.

dicular to this plane (see Fig. 2 of Ref. 6). The Hamiltonian $H^{\mathrm{I}^{(j)}\mathrm{Ar}^{(i)}}$ is then expressed in the coupled representation, $|JM\rangle$, according to a sequence of transformations analogous to those presented in Eqs. (2.6)–(2.12) of Ref. 6.

The Ar–I^- pair interactions are modeled by potentials constructed with the same short range interaction Hamiltonian presented above for the Ar–I fragment, supplemented with a long range attraction dominated by a $-1/r^4$ polarization term as detailed later in this subsection.

The *s*-ground state rare gas atoms interact according to a Lennard-Jones potential with $\epsilon=83.26\ \mathrm{cm}^{-1}$ and $\sigma=3.405$ Å.

The total Hamiltonian is written as the direct sum over all diatomic-fragment Hamiltonians as follows:

$$H=H^{(\mathrm{I}_2^-)}+\hat{\mathbf{1}}_2\otimes\left(\sum_{k=1}^{n}H^{\mathrm{I}^{(a)}\mathrm{Ar}^{(k)}}+\hat{\mathbf{1}}_6\otimes\sum_{k=1}^{n}V^{\mathrm{I}^-\mathrm{Ar}^{(k)}}\right)+\left(\sum_{k=1}^{n}H^{\mathrm{I}^{(b)}\mathrm{Ar}^{(k)}}+\hat{\mathbf{1}}_6\otimes\sum_{k=1}^{n}V^{\mathrm{I}^-\mathrm{Ar}^{(k)}}\right)\otimes\hat{\mathbf{1}}_2+\hat{\mathbf{1}}_{12}\otimes\sum_{i=1}^{n-1}\sum_{j>i}^{n}V^{\mathrm{Ar}^{(i)}\mathrm{Ar}^{(j)}},\tag{2.14}$$

where $\hat{\mathbf{1}}_n$ is the $n\times n$ unit matrix, and the constant monoatomic contribution appearing in Eq. (2.9) is omitted. The energy of the system is calculated relative to the energy of infinitely separated species in the ground state:

$$E_\infty=E_{\mathrm{I}[^2P_{3/2}]}+E_{\mathrm{I}^-[^1S_0]}+\sum_{j=1}^{N}E_{\mathrm{Ar}}.\tag{2.15}$$

As presented above, the diatomic terms $H^{(\mathrm{ArI}^-)}$ and $H^{(\mathrm{II}^-)}$ include the energy of polarization of neutral Ar and I atoms by the charged I^- anion. However, in order to take account of the self- consistent many-body nature of the electric field responsible for polarization we determine the energy of polarization in the electrostatic approximation separating it as a special perturbation term η_n,[48,54,55]

$$H_{mn,mn}=\langle\psi_{m,n}|\hat{H}|\psi_{m,n}\rangle=\sum_i\sum_{j>i}V_{\mathrm{Ar}^{(i)}\mathrm{Ar}^{(j)}}+\sum_j\left[\widetilde{V}_{\mathrm{I}^-\mathrm{Ar}_j}+\widetilde{V}_{\mathrm{I}_{J^{(n)}M^{(n)}}\mathrm{I}^-}\right]+\eta_n,\tag{2.16}$$

where the diagonal Hamiltonian matrix elements $H_{mn,mn}$ in Eq. (2.16) are written in the basis set of spaf's $\psi_{m,n}$ defined according to the following expression:

$$\psi_{m,n}=\chi_{m,n}\prod_{i=1}^{N}|s^{(i)}\rangle,\tag{2.17}$$

in which iodine atom n is the neutral open-shell species.

We approximate η_n by the classical expression for the energy of polarization as follows[56–58]

$$\eta_n=\sum_j\mu_j\frac{\mathbf{R}_{j\mathrm{I}^-}}{R_{j\mathrm{I}^-}^3}+\sum_j\sum_{i>j}\mu_j\cdot\mathbf{T}_{ij}\cdot\mu_i+\sum_j\frac{\mu_j\cdot\mu_j}{2\alpha_j}.\tag{2.18}$$

In Eq. (2.16) $\widetilde{V}$ is defined as

$$\widetilde{V}=V+\frac{C_4}{R^4},\tag{2.19}$$

where C_4 is expressed in terms of the atomic polarizability of the neutral atom, α, and the charge of the ion, q, as

$$C_4=\frac{1}{2}\,q^2\alpha.\tag{2.20}$$

For the calculation of η_n we consider atoms as nonoverlapping polarizable spheres and compute the induced dipole moments μ_j self-consistently according to the following equation:

$$\mu_k=\alpha_k\left[-\frac{\mathbf{R}_{k\mathrm{I}^-}}{R_{k\mathrm{I}^-}^3}-\sum_{j\neq k}\mathbf{T}_{jk}\cdot\mu_j\right]\tag{2.21}$$

where $\mathbf{T}_{jk}$ are the components of the dipole-dipole interaction tensor given by

$$T_{jk}=-\frac{3}{r^5}\begin{bmatrix}x^2-r^2/3 & xy & xz\\ xy & y^2-r^2/3 & yz\\ xz & yz & z^2-r^2/3\end{bmatrix},\tag{2.22}$$

where r is the interatomic distance with Cartesian components x, y, and z. The repulsive part of the Ar–I interaction is sufficiently steep so that geometries where this attractive polarization interaction diverges are never reached.

For each nuclear configuration we solve the system of equations defined by Eq. (2.21), compute the energy of polarization according to Eq. (2.18) and calculate the polyatomic energies by a simple diagonalization procedure requiring no electronic integral evaluations. The DIIS eigenvectors $\overline{\Gamma}_{kj}$ found by this diagonalization procedure define the VB wave functions of the system according to the following equation:

$$\phi_k(t)=\sum_{j=1}^{12}\overline{\Gamma}_{kj}\psi_j,\tag{2.23}$$

where index j abreviates the pair of indices mn presented in Eq. (2.16).

Potential energy curves calculated using the DIIS approach detailed above for a typical $\mathrm{I}_2^-\cdot\mathrm{Ar}_{17}$ cluster sampled from our ensemble of resonant initial configurations are presented in Fig. 4. These surfaces are computed by pulling the two iodine atoms apart symmetrically keeping the I_2^- center of mass position and bond orientation fixed at their initial values. For the solid curves the two capping argon atoms at the ends of the I_2^- molecule are moved apart in the same way thus as the two iodine fragments are pulled apart each single capping argon atom at either end of the I_2^- follows its iodine atom out as the bond is extended. All the other argon atoms which form the completed and partially completed rings surrounding the I_2^- bond are held fixed. For the dashed curves,

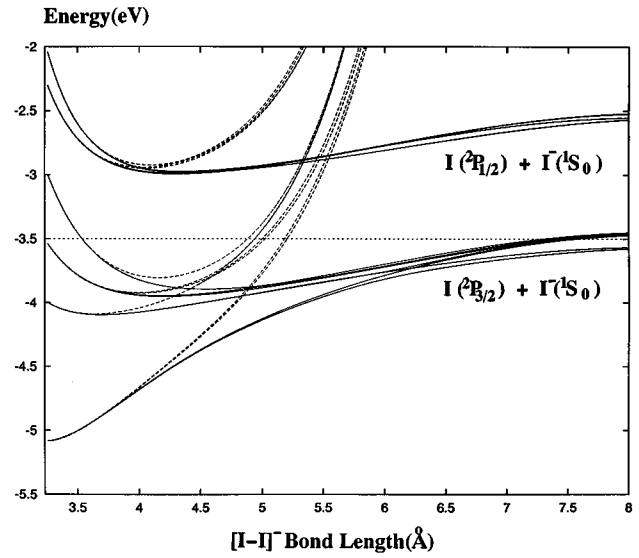

FIG. 4. Potential energy surfaces of $I_2^- \cdot Ar_{17}$ as functions of I_2^- bond length computed using the DIIS Hamiltonian with I_2^- center of mass position and bond orientation fixed at their initial values. For the solid curves the end capping atoms are moved out with the iodine fragments modelling cluster boundary conditions. Dashed curves show results computed with the capping atoms held fixed modelling rigid condensed phase boundary conditions.

on the other hand, all the argon atoms including the two capping atoms are held fixed as the I_2^- bond is extended. These two different bond extension schemes approximate the caging environment expected in the cluster (solid curve) in which the capping atoms are blasted off the cluster as the I_2^- bond is extended and in the frozen matrix (fixed capping atoms). Also overlayed on this figure is the A' state pump excitation energy, and the point where this excitation energy intersects the cluster like curves at around 7–7.5 Å indicates the expected turning point for the classical motion of the excited bond extension over these cluster surfaces.

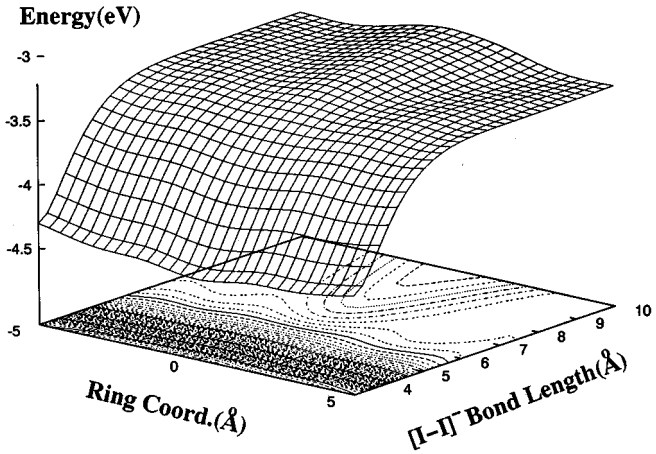

FIG. 5. Ground state potential energy surface obtained for $I_2^- \cdot Ar_6$ ionic molecular cluster system with the six Ar atoms in a ring configuration around the molecular axis. Surface is displayed as a function of ring coordinate along the molecular axis and I_2^- bond length.

Figure 5 shows the ground state potential surface calculated using the DIIS model for an artificial $I_2^- \cdot Ar_6$ cluster ion in which six argon atoms are located in a ring configuration of radius 4 Å around the molecular axis of the I_2^- molecule. The surface is plotted as a function of shifting the solvent ring along the I_2^- bond axis relative to its center of mass, for different I_2^- bond lengths. From this figure we see that for short I_2^- bond lengths the minimum energy configurations have the ring of argon atoms located in between the two I atoms, while for longer I_2^- bond lengths minimum energy configurations have the ring located near one or the other I atom. These features of the ground state PES can be understood in terms of the excess charge distribution of the molecule that goes from one equally shared between the two I near the equilibrium bond length to a charge stabilized by the surrounding solvent on one or the other I atom at larger internuclear separations.

D. Computation of approximate nonadiabatic coupling vectors, adiabatic forces and the adiabatic basis set propagator with DIIS

The nonadiabatic MD methods which we use to evolve the excited state dynamics of these cluster systems have been presented in detail elsewhere.[1–6] The adiabatic forces and nonadiabatic coupling vectors $\mathbf{D}_{mn}$ needed to implement these methods are computed in terms of the DIIS eigenvectors and diabatic Hamiltonian matrix elements using the following approximate results:[6,35]

$$\mathbf{D}_{mn} \approx -\frac{\Sigma_i \Sigma_j \overline{\Gamma}^*_{mi} \overline{\Gamma}_{nj} \nabla_{\mathbf{R}} \langle \Phi_i | H | \Phi_j \rangle}{(\epsilon_m - \epsilon_n)}, \tag{2.24}$$

$$\nabla_{\mathbf{R}} \epsilon_k \approx \sum_i \sum_j \overline{\Gamma}^*_{ki} \overline{\Gamma}_{kj} \nabla_{\mathbf{R}} \langle \Phi_i | H | \Phi_j \rangle, \tag{2.25}$$

where we have ignored terms like $\langle \nabla_{\mathbf{R}} \Phi_i | H | \Phi_j \rangle$ since the pbf's Φ_i are intended to reflect only gradual distortions so they vary slowly with nuclear configuration. These same ideas have proved very valuable for describing low-energy molecular collision processes[49] (and Refs. 20, 24, 29, and 32 therein).

As an independent test of the approximations underlying the above result (the slow variation of the pbf's with nuclear coordinates) we have computed the forces by finite difference estimation using variation of the DIIS eigenvalues and find that the force obtained from Eq. (2.25) is very accurate for typical fluid configurations.

The gradients of the DIIS Hamiltonian matrix elements in the pbf basis set in Eq. (2.25) or Eq. (2.24) are most conveniently computed using finite difference, although they can be computed exactly as indicated above by differentiating the necessary transformation matrices and the empirical potential energy matrices. For every interacting pair a new set of matrices and the necessary derivatives need to be computed and multiplied. We find that a three point finite difference approach is accurate and comparable in computational expense, and much easier to code for general applications.

However, the gradient of the polarization term, $\nabla_{\mathbf{R}}\eta_n$, is calculated analytically according the following expressions:

$$\frac{\partial \eta_n}{\partial \mathbf{R}_p} = -\mu_p \left[\frac{\partial \mathbf{E}_{np}}{\partial \mathbf{R}_p} - \sum_{j \neq p} \frac{\partial \mathbf{T}_{jp}}{\partial \mathbf{R}_p} \mu_j \right], \tag{2.26}$$

$$\frac{\partial \eta_n}{\partial \mathbf{R}_c} = -\sum_j \mu_j \frac{\partial \mathbf{E}_{cj}}{\partial \mathbf{R}_c}, \tag{2.27}$$

where $\mathbf{R}_p$ and $\mathbf{R}_c$ represent the coordinates of the dipoles and the charge, respectively.

The final quantity we need to implement the surface hopping nonadiabatic algorithm is the electronic subsystem propagator which we compute in terms of the DIIS eigenvectors and eigenvalues ϵ_n as described in Ref. 6 according to:

$$\mathbf{T}_{no}(t+\delta,t) \approx \exp\left[\frac{-i\delta}{2\hbar} (\epsilon_n(t+\delta) + \epsilon_o(t)) \right] \sum_i \Gamma^*_{ni}(t+\delta) \Gamma_{oi}(t). \tag{2.28}$$

III. RESULTS

A. General overview of experimental observations

In the experiments of Vorsa *et al.*,[25] photoexcitation of I_2^- in argon clusters, $I_2^- \cdot Ar_i$ (where there are i argon atoms solvating the I_2^- in the initially prepared unexcited cluster, $0 \leqslant i \leqslant 27$), leads to various charged fragmentation products which are detected using mass spectrometry:

(1) The I_2^- molecular anion can dissociate in the cluster, loosing an I radical, and evaporating argon solvent atoms yielding detectable $I^- \cdot Ar_f$ photofragments;
(2) Alternatively, for large enough clusters, the dissociating fragments of the I_2^- ion can be effectively caged by the surrounding cluster atoms, lose some of their excitation energy and recombine to form a stable, possibly excited molecular anion.

In the latter case the caging interactions that give rise to energy loss from the excited I_2^- result in evaporation of argon solvent atoms giving detectable $I_2^- \cdot Ar_{f'}$ fragments. Vorsa *et al.* analyze their experimental results in terms of the excess excitation energy being deposited into the surrounding solvent and resulting in evaporation of atoms from the cluster. Their analysis gives a mean binding energy per evaporated solvent atom and correlates well with the product photofragment size distributions they observe.

Depending on the excitation energy, and the prepared initial cluster size, i, different charged product photofragment distributions $P(f)$ are observed. For example, with a 790 nm excitation which takes the I_2^- from its ground X, $^2\Sigma^+_{u,1/2}$ state to the excited A', $^2\Pi_{g,1/2}$ state in the Franck–Condon region, the experiments reveal that for precursor clusters with less than $i \sim 10$ argon atoms solvating the I_2^- ion, solvent caging is ineffective and we see only dissociated photofragments of the form $I^- \cdot Ar_f$ where the distribution of final cluster sizes, $P(f)$, covers the range from $f \sim 0$ to $f \sim i/2$, i.e., as many as half the argon atoms in the precursor cluster can be evporated during dissociation. However, the average charged product photofragment under these dissociative conditions is $I^- \cdot Ar$ (i.e., $f \sim 1$).

As the precursor cluster size is increased beyond $i \sim 10$ argon atoms, the $I^- \cdot Ar_f$ product channel closes down rapidly and by about $i \sim 16$ the only photofragments observed involve the recombined molecular anion and are of the form $I_2^- \cdot Ar_{f'}$. In the transitional precursor cluster size range between $i = 10$ and 16 argon atoms we see a mixture of dissociated ($I^- \cdot Ar_f$) and recombined ($I_2^- \cdot Ar_{f'}$) photofragments. In this precursor size range, the dissociated photofragment product distribution splits into two subdistributions: A small cluster band in which the I^- is solvated by $f = 0$, 1, 2 or 3 argon atoms, the dominant average cluster being $I^- \cdot Ar$ independent of precursor cluster size, and a larger cluster band ($f = 5$, 6 or 7) whose major component is the $I^- \cdot Ar_6$ cluster but the average cluster size in this band scales linearly with precursor size.

The recombined product ($I_2^- \cdot Ar_{f'}$) photofragment size distributions for precursor cluster sizes $i > 10$ show characteristic bimodal shapes with a persistent peak at $f' = 0$, and a band of peaks whose mean size shifts linearly to larger terminal recombined clusters as the precursor cluster size i is increased. Vorsa *et al.* interpret these two distinct classes of recombined photofragments as arising from two different recombination pathways, as follows.

(a) The photofragments of the dissociated I_2^- molecule are effectively caged by the solvating cluster so that they recombine into the ground X, $^2\Sigma^+_{u,1/2}$ electronic state with a large amount of residual vibrational excitation. As this recombined ground state molecular anion vibrationally relaxes its excess energy is dumped efficiently into the surrounding cluster resulting in all the argon atoms of the intermediate size precursor clusters being evaporated and giving rise to the strong peak at $f' = 0$ in the recombined photofragment size distribution.

(b) Alternatively, Vorsa *et al.* argue that the recombination can either occur with significant rearrangement of the cluster producing a metastable solvent separated ground state configuration, or the I_2^- can recombine into an excited electronic state. Both these recombination pathways result in evaporation of argon atoms. However, because some of the excess energy is still tied up in either electronic excitation, or in the metastable solvent separated ground state configuration, not all the argon atoms are evaporated. This results in the distribution of larger recombined photofragments for these intermediate precursor clusters.

B. Detailed comparison of calculations and experimental results

As outlined in Sec. II A, for reasons of economy we have used only 18 trajectories in our nonadiabatic MD ensembles for these cluster systems. These trajectories had to be followed for relatively long times to reach their equilibrium sizes after photoexcitation, and a broad range of precursor cluster sizes had to be surveyed. In our previous studies of photodissociation of I_2 in liquid and solid rare gases[35]

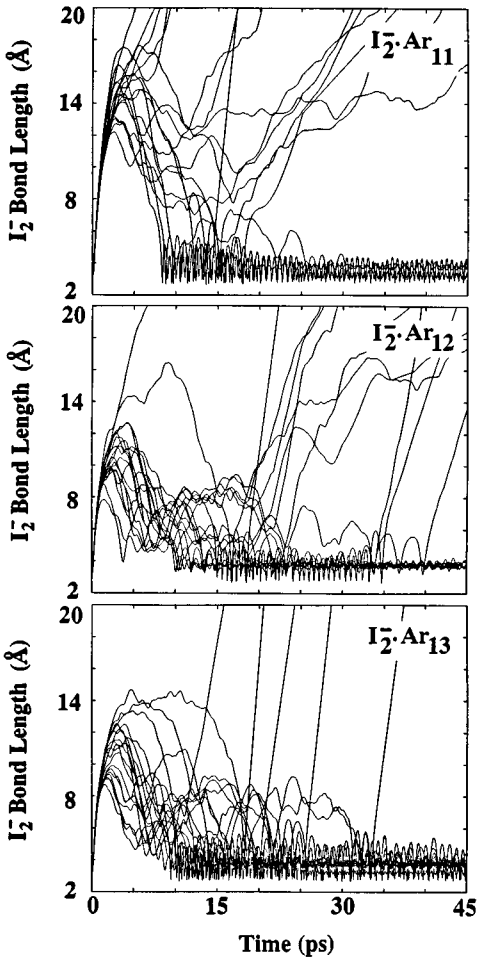

FIG. 6. I—I bond length histories for various ensembles of 18 nonadiabatic MD trajectories for the $i=$ 11, 12 and 13 precursor cluster systems.

we averaged our results over four different ensembles, each of 18 trajectories giving a total ensemble size of 72 trajectories. In these studies we found that the number of trajectories branching into the different possible nonadiabatic channels, and the general qualitative features of the results computed for the full ensemble were reliably represented by each subensemble of only 18 trajectories. We thus believe that our cluster results presented here for these relatively small ensembles give a reliable qualitative overview of cluster photodissocitation processes. Calculation of precise details of the size distributions etc., would require larger ensemble sizes and are beyond the scope of these survey studies.

In Sec. II B we described the underlying equilibrium structure of the I_2^- solvation shell for the small to intermediate size argon clusters predicted by our DIIS ground state potential surface. In an attempt to develop an understanding of how these underlying precursor cluster structures influence the photofragmentation dynamics and ultimately the product photofragment size distributions observed experimentally, in Fig. 6 we display the I—I bond length histories for various ensembles of 18 nonadiabatic MD trajectories of the $i=11$, 12 and 13 atom precursor cluster systems. The initial configurations were sampled from equilibrium ground state distributions at $T=40$ K. The initial energy gap between the X and A' states of the different ensemble members for each cluster size is resonant with the 790 nm pump pulse. At $t=0$ all members of a given ensemble are excited to the A' electronic state and the ensuing many-body nonadiabatic dynamics is followed using surface hopping methods.

The most striking feature evident from the trajectories displayed in Fig. 6 is that as the precursor cluster size is increased from $i=11$ to $i=13$ argon atoms, trajectories in which the two iodine fragments simply separate ballistically on the repulsive excited electronic state are prominent for the $i=11$ atom precursor cluster, while they are not observed at all for the $i=13$ atom cluster or for any precursor clusters larger than this (see Fig. 9). On the other hand, precursor clusters smaller than $i=11$ all exhibit the ballistic dissociation channel in which the I atoms simply fly apart largely unperturbed by the surrounding cluster. The dissociation dynamics of these smaller clusters is dominated by this behavior.

The reason for this extreme sensitivity of the trajectories to precursor cluster size in this range is apparently due to the relative stability of clusters with a hexagonal ring of argon atoms around the I—I bond compared to clusters which do not exhibit this structural motif. From Fig. 2 we see that the equilibrium geometry of the $i=11$ atom cluster has an incomplete ring of only 5 argon atoms about the I—I bond while the cap of this cluster also has an incomplete 5 membered ring topped by a single atom. When we increase the cluster size to $i=12$ and 13 argon atoms (or larger than this) we complete the 6 membered ring around the I—I bond giving a very stable solvating structure. As the two iodine fragments fly apart after electronic excitation in the $i=13$ atom precursor cluster, for example, this symmetrical ring structure remains intact. The charges on the departing iodine fragments polarize this stable ring leading to symmetrical long range attractive forces which cause all the I—I bond trajectories for this precursor cluster size to show a broad distribution of turning points at between $\sim$8.5 Å and $\sim$14 Å (see Fig. 6). The stable central ring thus acts as an attractor which initiates the recombination of the molecular anion. For the $i=11$ atom precursor cluster, on the other hand, when the excited iodine fragments leave the cluster on the first bond extension the 5 membered bond ring is more often destabilized and the remaining cluster of solvent breaks apart leaving no center for attraction of the separating iodine fragments which simply dissociate.

Since even partially completed ring structures show the underlying hexagonal shape in the minimum energy cluster geometries shown in Fig. 2, unfinished rings with only 4 atoms have very open, half completed hexagonal structures. When the I_2^- flies apart after photoexcitation and the iodine fragments leave the smaller clusters which show these open structural features, the unstable half completed rings will break apart, fragmenting the solvent cluster so there will be no attractor site to nucleate I_2^- recombination. As soon as we have a ring structure in the cluster which is beyond half complete, with say 5 atoms, the additional atom seems to be able to partially stabilize the ring so that it can remain intact

after initial photofragmentation of the I_2^- and can thus be partially effective in nucleating recombination of the I_2^- fragments. From Fig. 2 we see that the first cluster which shows a 5 member or more, over half complete hexagonal ring structure is the $i=10$ atom precursor cluster and we believe that this is the reason that this is the first cluster which shows detectable I_2^- recombination fragments in both the experiments and in our calculations.

From the bond length trajectories of the $i=12$ and 13 atom precursor clusters in Fig. 6 we see that the return of the iodine fragments can result in I_2^- recombination characterized by the highly oscillatory bond length trajectories, or alternatively as the iodine fragments return to the cluster, if some of the solvent atoms have been dislodged, the recoiling iodine fragments may collide with these displaced solvent atoms which destroys the solvent cluster resulting in the iodine fragments dissociating permanently.

For our trajectories which show effective recombination and persistant oscillation of the I_2^- bond length at long times we see two distinctively different types of possible vibrational motion characterized by different frequencies, amplitudes and equilibrium bond lengths. These different vibrational motions result from recombination either into the ground X electronic state of the cluster which, as we see in Fig. 6, is characterized by a higher frequency and shorter equilibrium bond length ($R_X^{\mathrm{eq}}\sim 3.25$ Å), or recombination into the excited A state and from Fig. 4 this surface is bound in the cluster, and it is characterized by a lower vibrational frequency and its equilibrium I—I separation is nearly 0.5 Å longer than in the cluster ground state with $R_A^{\mathrm{eq}}\sim 3.75$ Å. The trajectories for the $i=13$ atom cluster displayed in Fig. 6 show examples of recombination which yields vibrationally hot recombined I_2^- molecules in which the electronic excitation is converted into large amplitude vibrational motion on the electronic ground state as well as smaller amplitude vibrations whose equilibrium bond length is characteristic of recombination into the excited A state of the cluster. In addition we see a trajectory which recombines into the ground state and loses a large amount of vibrational excitation presumably through efficient coupling to translational motion of the argon atoms which could be kicked off the cluster at high speeds.

Clearly the precise amount of branching into these different types of photoproduct channels as a function of precursor cluster size will be very sensitive to the accurate treatment of the dissociation dynamics of these clusters. Thus prediction of terminal product distributions for these photofragmentation reactions in clusters provides a very stringent test for our nonadiabatic dynamics methodologies and the interaction potentials obtained from our DIIS calculations. In Figs. 7 and 8 we thus present a detailed comparison of the photofragment product distributions for the $i=13$ precursor cluster. Due to the partial capping, discussed earlier, this cluster is in the transitional precursor size range and thus its photofragment distribution shows a particularly rich array of varied product channels. Even with our ensembles of only 18 trajectories the product distributions for the $I_2^-\cdot Ar_{f'}$ fragmentation channel (see Fig. 8) obtained from our calculations are in remarkably good qualitative agreement with the experimental results. We do not have the statistics to resolve the $I^-\cdot Ar_f$ channel (see Fig. 7) into the various possible photofragments as only 5 of our trajectories actually dissociated this way but the relative proportion of this channel compared to the recombination pathway is well reproduced and we do see evidence of the split distribution observed experimentally for these channels.

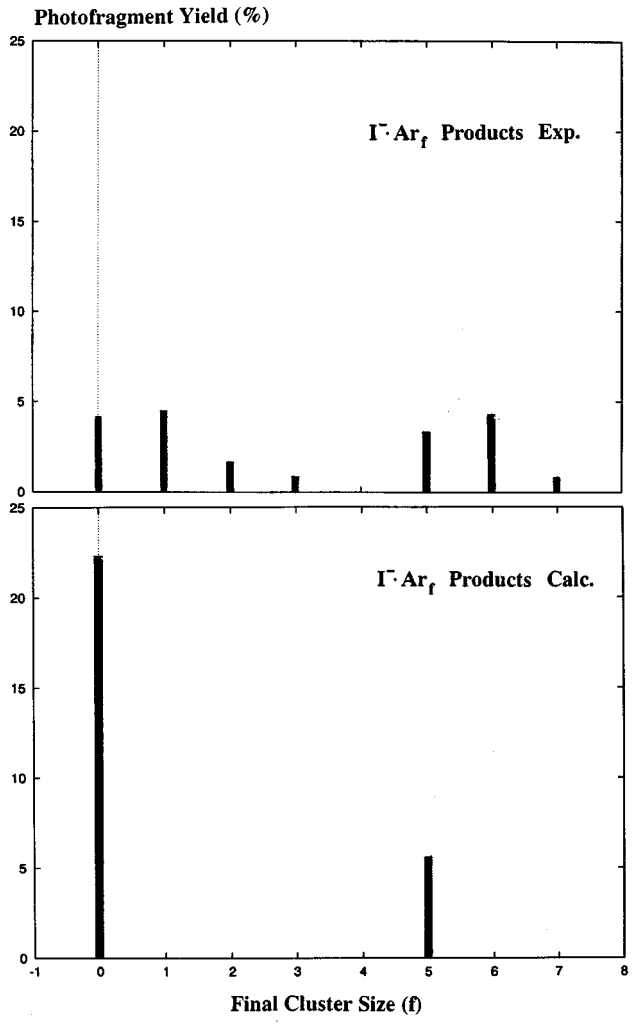

FIG. 7. Histogram of the $m/e=127$-based ionic photofragments (uncaged) $I^-\cdot Ar_f$ from $I_2^-\cdot Ar_{13}$ precursor cluster after photoexcitation at $\lambda=790$ nm. The upper graph displays experimental values while the lower graph shows nonadiabatic MD simulation results.

In Fig. 9 we present similar bond length trajectory plots for larger precursor cluster sizes, $i=15$, 17 and 19 argon atoms. There are two related features to note when comparing these larger cluster results with those presented in Fig. 6 for the smaller clusters $i=11$, 12 and 13: First, we see that the trajectories which dissociate after being attracted back to the cluster and colliding with displaced solvent atoms rapidly drop out of our ensemble over this larger cluster size range and only represent about 10% of trajectories at $i=17$ and they are completely absent by the $i=19$ argon atom cluster. This indicates that the argon atoms around the body of the

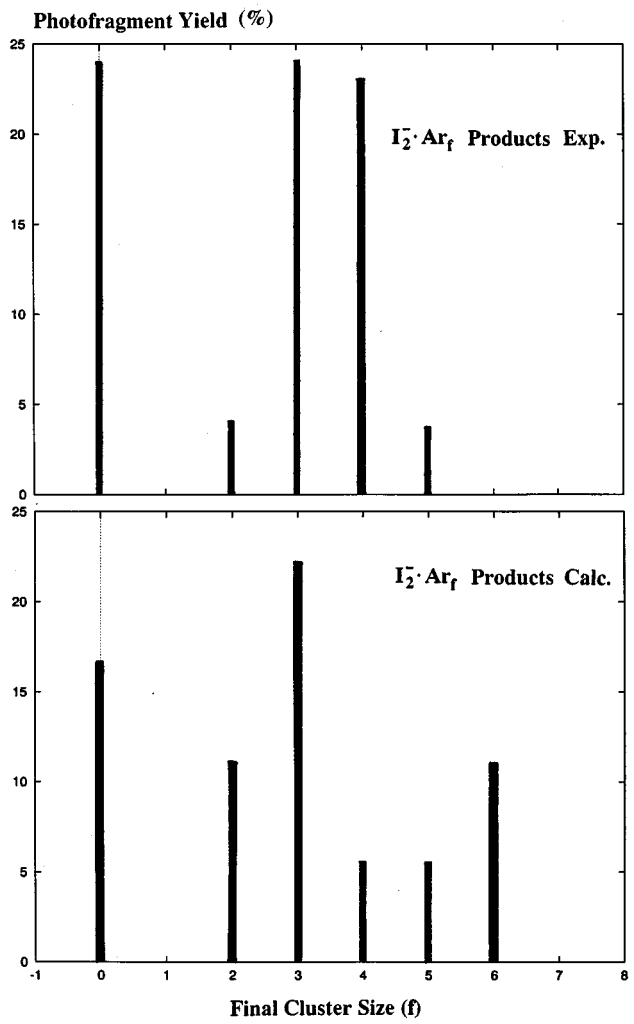

FIG. 8. Same as Fig. 7 but for $m/e=254$-based recombined ionic photofragments $I_2^-\cdot Ar_{f'}$.

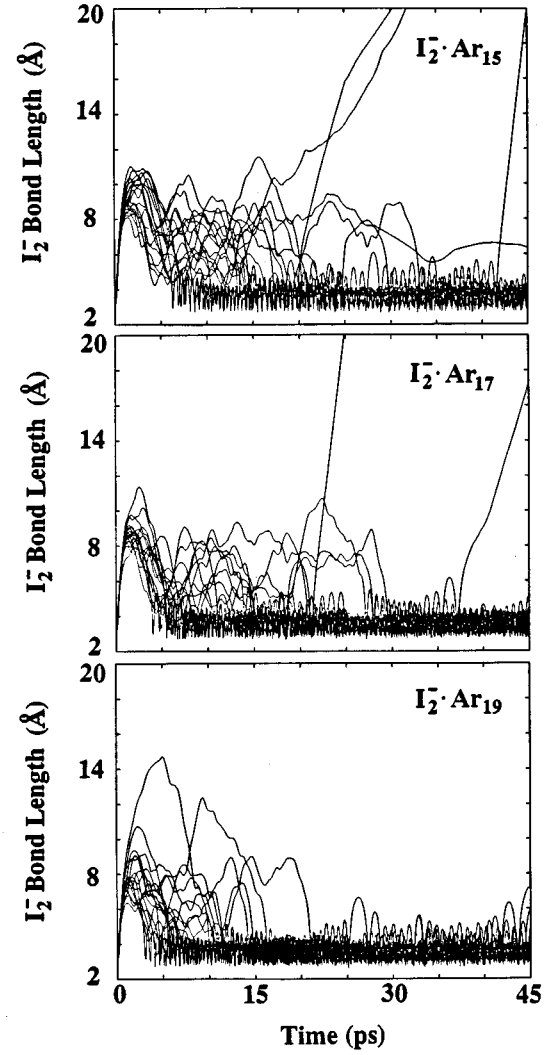

FIG. 9. I–I bond length histories for various ensembles of 18 nonadiabatic MD trajectories of the $i=15$, 17 and 19 precursor cluster systems.

cluster are held in place more rigidly for these larger precursor clusters and are thus less able to be dislodged as a result of the first I_2^- bond extension.

The second intriguing feature evident when comparing these trajectory plots for the various clusters is the dramatic effect precursor cluster size has on the attractive interactions responsible for turning the trajectories around and bringing the iodine fragments back toward the solvent cluster and possible recombination. We see the mean turning points vary from about 14 Å for the $i=11$ atom cluster to only about 7 Å for the $i=19$ precursor cluster. It is evident from the trajectories that these smaller bond excursions in the larger, more stable and more strongly attractive clusters decrease the time scale for recombination by about a factor of 3 being roughly 10 ps before the first characteristic bound vibrations for the $i=13$ atom cluster and considerably less than 5 ps for the $i=19$ precursor cluster. As the number of tightly localized charge induced dipoles in the more rigidly held atoms of the larger clusters increases, the attractions responsible for the recombination also increase significantly. Pump-probe experiments[24] for I_2^- in CO_2 clusters indicate longer absorption recovery times ($\sim 10-30$ ps) than those we see above for our calculations in argon clusters. It would be interesting to see if this prediction is verified in dynamical experiments on argon clusters. The CO_2 experiments do show the same sigmoidal decreasing trend in recovery time with increasing cluster size apparent from our results in argon clusters.

In Fig. 10 we present our calculated recombined fragment distributions which exhibit the characteristic bimodal evolution with precursor cluster size similar to that observed in the experiments. This bimodal distribution, with its strong peak at $f'=0$ and group of fragmentation peaks whose average size increases linearly with precursor cluster size in close agreement with the experimental results presented by Vorsa *et al.*,[25] results due to the two different nonadiabatic recombination channels evident in the bond length trajectory plots discussed earlier. When the I_2^- recombines rapidly into its ground X electronic state and exhibits high frequency, large amplitude vibrational motion, the excess excitation energy in this vibrational motion can be efficiently coupled into evaporation of solvent atoms as the highly vibrationally ex-

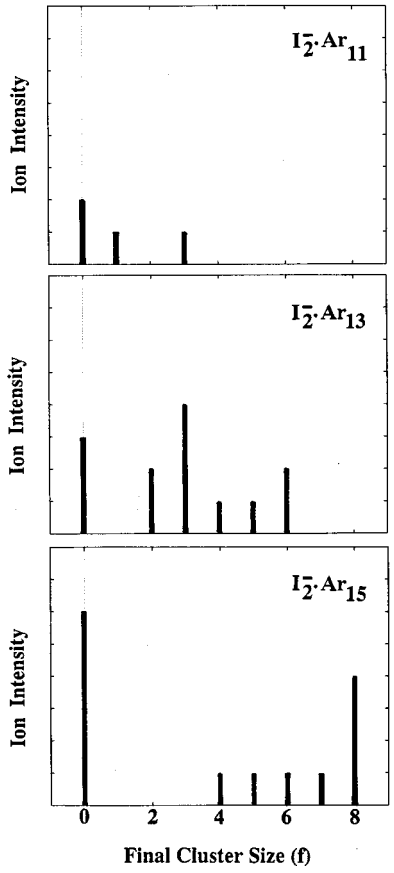

FIG. 10. Histograms of the recombined ionic photofragments $I_2^-\cdot Ar_{f'}$ for precursor clusters $I_2^-\cdot Ar_i$ ($i=$ 11, 13 and 15) after photoexcitation at $\lambda=790$ nm. This plot exhibits the two classes of $m/e=254$-based photoproducts also observed in experiments. The average separation between the two distributions increases with the cluster size.

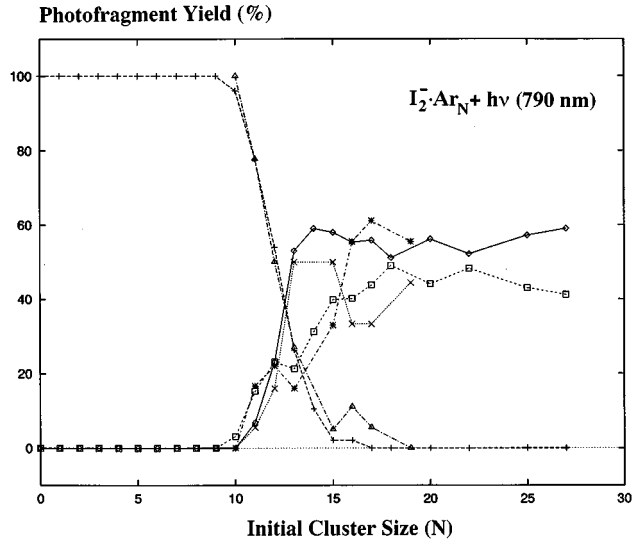

FIG. 11. Comparison of calculated and experimental normalized branching ratios for the three distinct photoproduct channels: $I^-\cdot Ar_f$ (uncaged), + symbols (expt.) and triangles (calc.), bare I_2^- (caged, and recombined into the ground X electronic state), squares (expt.) and stars (calc.), and $I_2^-\cdot Ar_{f'}$ (caged, and recombined into the excited A electronic state), diamonds (expt.) and crosses (calc.).

cited molecular anion attempts to undergo vibrational relaxation. For these intermediate size clusters this vibrational relaxation can lead to evaporation of all the solvent atoms giving the strong peak at $f'=0$. Recombination into the excited A electronic state, on the other hand, leaves a substantial part of the photon energy locked up in electronic excitation thus these recombined electronically excited trajectories exhibit smaller amplitude, lower frequency vibrations which are ineffective at coupling energy into evaporation of solvent atoms from the cluster. This recombination channel thus gives rise to the group of larger product cluster bands which shift with increasing precursor cluster size due to the fact that there are simply more atoms to start with and the same, relatively small, amount of excited state vibrational energy to unload into evaporation.

We follow the experimental workers[25] and summarize the results of our calculations by plotting the percentage photofragment yields of $I^-\cdot Ar_f$ (''uncaged''), bare I_2^- (''caged'', and recombined into the ground X electronic state) and $I_2^-\cdot Ar_{f'}$ (so-called ''solvent separated,'' which we interpret as recombination into the excited A electronic state). A comparison of our calculated component yields with those obtained from experiments is presented in Fig. 11.

Considering the approximations underlying our nonadiabatic MD methods and our semiempirical DIIS calculations of the excited electronic state surfaces, combined with the small ensemble sizes used in these studies, the agreement between the calculated and experimental photofragment yields is remarkable.

The sudden closing of the $I^-\cdot Ar_f$ uncaged channel is well represented in our calculations, and except for the fact that this photoproduct persists in small yields out to about $i=17$, our calculated trends are in almost quantitative agreement with experiment. The growing in of the caged I_2^- photoproduct yield above $i=10$ is also in nearly quantitative agreement with the experimental curve up to the precursor cluster size of $i=15$. Even the peak at $i=12$ and the small drop at $i=13$ are well described in our calculations. The calculations predict too much caged photoproduct for $i>15$ but our calculated results never deviate from the experimental curves by more than 10%. The establishment of the $I_2^-\cdot Ar_{f'}$, solvent separated (excited state recombined) photoproduct is also extremely will represented in our calculations which correctly predict even the oscillatory trend with increasing precursor cluster size. The yield of excited state recombined product is slightly underestimated in our calculations, but again it never deviates from the experimental results by more than 10%.

The branching of trajectories into the X or A states, and thus the photofragment yields of the different product clusters in these experiments, is directly controlled by the electronic nonadiabatic dynamics of these excited state systems. This branching is sensitive to the details of the electronic coupling between the states, and the speed with which the classical nuclear coordinates move through the coupling re-

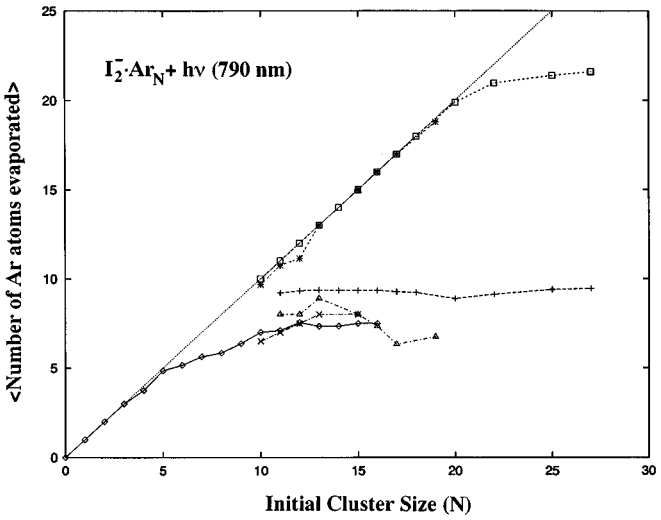

FIG. 12. Average number of Ar atoms evaporated for the uncaged in diamonds (expt.) and crosses (calc.); caged recombined into the X state in squares (expt.) and stars (calc.); and recombined into the excited A state in plus signs (expt.) and triangles (calc.).

gions. The fact that our calculated yields of the different photofragments are so close to the experimental results given this sensitivity gives us confidence in our methodology.

As a final comparison with experiment, in Fig. 12 we plot an even more demanding quantity, the average number of argon atoms evaporated from the cluster as a function of precursor size for the different product channels. The curve for the $I^- \cdot Ar_f$ photoproduct thus represents the number of atoms that do not bind to the iodide ion after the I_2^- molecular anion dissociates and breaks apart the cluster. This is a particularly challenging quantity to calculate and our results are in extraordinary agreement with experiment.

For intermediate size clusters out to $i=20$ the ground state recombination channel leads to evaporation of all the cluster atoms as a result of vibrational relaxation and efficient energy transfer to the solvent. Above $i=20$ the experiments indicate that the vibrational relaxation is completed so unevaporated solvent atoms begin to remain attached to the vibrationally relaxed I_2^-, and the number of evaporated atoms begins to level off at about 22. We begin to see evidence of this effective vibrational relaxation in our calculations by $i=19$ as some of our ensemble members still have an argon atom attached to the I_2^- ion after 45 ps.

For the final excited A state recombination channel we see that our calculations predict that there are too few argon atoms being evaporated from the cluster (only ~ 7) compared with experimental results (~ 9). This difference could be due to the fact that because the excited state surface is particularly shallow the relaxation on this surface is very slow and our 45 ps trajectories are not long enough to see all the evaporation that takes place at longer times in the experiments. We also ignore the possibility of fluorescence from these recombined electronically excited clusters in our calculations. If clusters do indeed equilibrate on the A state surface as a result of early evaporation of cluster atoms then, because of the longer bond length shift in the minimum of the excited state relative to the ground state apparent in the cluster potential curves of Fig. 4, radiative relaxation of the $I_2^- \cdot Ar_{f'}$ cluster will leave the I_2^- slightly vibrationally hot on the ground electronic state, thus more atoms may be evaporated after radiative relaxation, giving evaporation results in closer agreement with experiment. Indeed assuming a Franck–Condon photodeexcitation from the minimum of the excited cluster A state shown in Fig. 4 indicates that there would be roughly ~ 0.15 eV excess vibrational excitation after dropping to the ground state due to the displacement of the equilibrium positions of these surfaces. The subsequent evaporation of two more cluster atoms after fluorescence is thus consistent with the roughly ~ 70 meV binding energy per atom estimated from the experimental studies.[25]

IV. CONCLUSIONS

In order to address the role of electrostatic interactions on the dynamics of chemical reactions in cluster systems, DIIS methods were combined with a nonadiabatic surface hopping algorithm in simulations of ultrafast pump photoexcitation experiments on the photodissociation, geminate recombination and vibrational relaxation of I_2^- in size selected $I_2^- \cdot Ar_n$ ionic molecular clusters. For reasons of economy, the ensemble sizes used in these calculations are fairly small and we could realistically only run the calculations out to relatively short times compared to flight times of the experiments. Despite these limitations we believe our results are meaningful and our calculated photofragment yields of different ionic products are found to compare remarkably well with recent experiments by Vorsa *et al.* on this system.

Our nonadiabatic MD simulations showed that the dynamics of relaxation of both the chromophore and the solvent are intimately coupled. The various potential surfaces of the chromophore that participate in the dynamics of relaxation are coupled by the presence of the surrounding particles. These couplings generate electronic relaxation of the chromophore into excited nuclear vibrational states of lower lying electronic surfaces and the excess kinetic energy of the chromophore thus generated is absorbed by the solvent which undergoes partial or total evaporation from the cluster. The dynamics of photodissociation and geminate recombination in $I_2^- \cdot Ar_n$ ionic molecular clusters exhibited strong cluster size dependence in the range $10 \leqslant n \leqslant 15$ and recombination times decrease with increasing cluster size, in agreement with general experimental findings.[20,24] Comparing our calculations in argon with the experiments in CO_2 we predict that recombination dynamics is roughly a factor of 2–3 times faster in argon than in CO_2 and more experimental and theoretical work is necessary to verify and understand these differences.

The branching ratios and the photofragment yields of the different product clusters obtained from our nonadiabatic MD simulation methods coupled to DIIS electronic structure calculations are in almost quantitative agreement with experimental results and provide important documentation on the ability of these computational techniques to simulate the

detailed the influence of the solvent on the dynamics of chemical reactions in condensed phase like environments.

The electronically nonadiabatic recombination dynamics which is ultimately responsible for branching into different photofragment products and controls the amount of cluster evaporation is driven by long range charge-induced dipole interactions in these clusters. In the traditional solution phase interpretation of these recombination phenomenon the term caging is usually understood to describe the very short ranged repulsive interactions that the dissociating fragments are subject to as they collide with the unrelenting mass of surrounding solvent atoms and recoil off the walls of this solvent cage to again find one another and possibly recombine as a result of energy loss during these early solvent collisions.

The picture of the caging phenomenon we find in these charged chromophore cluster systems is dramatically different: The short range interactions are only active for a fleeting moment as the two capping argon atoms at the ends of the cluster recoil with high velocities after suffering almost impulsive collisions with the ballistic iodine fragments. Due to the large mass difference between the iodine and argon atoms, the iodine fragments still have momentum and continue to move outward from the cluster but their speeds are greatly reduced and are now less than the escape velocity needed for the strong attractive charge-induced dipole forces which operate at larger distances in these systems. Provided the remaining cluster has not broken up too much as a result of the initial departure of the iodine fragments, the largest piece of the remaining cluster, with the biggest induced dipole, may then act as a long range attractor for the iodine fragments which may subsequently find one another in the region of this cluster and recombine through various nonadiabatic channels. In these clusters the short range interactions are thus only active to slow the escaping photofragments so that long range forces can drag them back together.

As the cluster size is increased toward the bulk phase in contrast, we expect that deep within a large cluster the long range forces provide little more than an over all background off set to the total energy which changes slowly as we move through the bulk. The more traditional view of photofragment caging dictated by the rapidly changing short range part of the potential again emerges. Long range interactions may be important for recombination processes in intermediate size clusters if the chromophore finds itself near the surface of the cluster. In a future publication[59] we will explore these different roles of long and short range interactions and their effects on ultrafast pump-probe signals from photodissociating I_2^- in both the liquid and solid phases.

The final point to reiterate here is that our simulations reveal that when the precursor cluster is large and stable enough to promote recombination of the iodine fragments we observe reformation of the I_2^- bond via two different channels: The I_2^- molecule can either recombine into the ground electronic state in which case it can be highly vibrationally excited and the subsequent vibrational relaxation can result in evaporation of many cluster atoms. Alternatively the I_2^- may initially recombine into the excited A state in which low frequency motions are ineffective at coupling energy into solvent atom evaporation giving rise to larger recombined clusters which may also survive radiative deexcitation at longer times. In this excited electronic state of the entire cluster, analysis of recombined configurations reveals that there is a tendency for argon atoms to group about the region of the bond but we do not see excited state configurations that could realistically be described as solvent separated.[25] Similarly we do not see evidence of metastable recombined configurations in the ground electronic state which involve solvent separation in these small to intermediate size clusters.

ACKNOWLEDGMENTS

We gratefully acknowledge financial support for this work from the National Science Foundation (Grants No. CHE-9058348 and No. CHE-9521793), the Petroleum Research Fund administered by the American Chemical Society (Grant No. 27995-AC6) and a generous allocation of supercomputer time from Boston University's center for Scientific Computing and Visualization.

[1] J. C. Tully, J. Chem. Phys. **93**, 1061 (1990).
[2] S. Hammes-Schiffer and J. C. Tully, J. Chem. Phys. **101**, 4657 (1994).
[3] D. F. Coker, in *Computer Simulation in Chemical Physics*, edited by M. P. Allen and D. J. Tildesley (Kluwer, Dordrecht, 1993), pp. 315–377.
[4] H. S. Mei and D. F. Coker, J. Chem. Phys. **104**, 4755 (1996).
[5] D. F. Coker and L. Xiao, J. Chem. Phys. **102**, 496 (1995).
[6] V. S. Batista and D. F. Coker, J. Chem. Phys. **105**, 4033 (1996).
[7] J. M. Farrar, in *Current Topics in Ion Chemistry and Physics*, edited by C. Y. Ng and I. Powis (Wiley, New York, 1992).
[8] T. Baumert, C. Rottgerman, C. Rothenfusser, T. Thalweiser, V. Weiss, and G. Gerber, Phys. Rev. Lett. **69**, 1512 (1992).
[9] J. J. Breen, D. M. Willberg, M. Gutman, and A. H. Zewail, J. Phys. Chem. **93**, 9180 (1990).
[10] C. A. Schmuttenmaer, J. Qian, S. G. Donnelly, M. J. DeLuca, D. F. Varley, L.A. DeLouise, R. J. D. Miller, and J. M. Farrar, J. Phys. Chem. **97**, 3077 (1993).
[11] J. Steadman, E. W. Fournier, and J. A. Syage, Appl. Opt. **29**, 4962 (1990).
[12] S. Wei, J. Purnell, S. Buzza, R. J. Stanley, and A. W. Castleman, Jr., J. Chem. Phys. **97**, 9480 (1992).
[13] I. R. Sims, M. Gruebele, E. D. Potter, and A. H. Zewail, J. Chem. Phys. **97**, 4127 (1992).
[14] M. Gruebele, I. R. Sims, E. D. Potter, and A. H. Zewail, J. Chem. Phys. **95**, 7763 (1991).
[15] N. F. Scherer, L. R. Khundkar, R. B. Bernstein, and A. H. Zewail, J. Chem. Phys. **87**, 1451 (1987).
[16] S. I. Ionov, G. A. Brucker, C. Jacques, L. Valachovic, and C. Wittig, J. Chem. Phys. **97**, 9486 (1992).
[17] J. J. Breen, L. W. Peng, D. M. Willberg, A. Heikal, P. Cong, and A. H. Zewail, J. Chem. Phys. **92**, 805 (1990).
[18] M. F. Hineman, G. A. Brucker, D. F. Kelly, and E. R. Bernstein, J. Chem. Phys. **97**, 3341 (1992).
[19] J. A. Ayala, W. E. Wentworth, and E. C. M. Chen, J. Phys. Chem. **85**, 768 (1981).
[20] J. M. Papanikolas, J. R. Gord, N. E. Levinger, D. Ray, V. Vorsa, and W. C. Lineberger, J. Phys. Chem. **95**, 8028 (1991).
[21] M. L. Alexander, M. A. Johnson, N. E. Levinger, and W. C. Lineberger, J. Chem. Phys. **88**, 6200 (1988).
[22] D. Ray, N. E. Levinger, J. M. Papnikolas, and W. C. Lineberger, J. Chem. Phys. **91**, 6533 (1989).
[23] J. M. Papanikolas, V. Vorsa, M. E. Nadal, P. J. Campagnola, and W. C. Lineberger, J. Chem. Phys. **97**, 7002 (1992).
[24] J. M. Papanikolas, V. Vorsa, M. E. Nadal, P. J. Campagnola, H. K. Buchenau, and W. C. Lineberger, J. Chem. Phys. **99**, 8733 (1993).

[25] V. Vorsa, P. J. Campagnola, S. Nandi, M. Larsson, and W. C. Lineberger, J. Chem. Phys. **105**, 2298 (1996).
[26] C. J. Delbecq, W. Hayes, and P. H. Yuster, Phys. Rev. **121**, 1043 (1961).
[27] J. M. Papanikolas, V. Vorsa, M. E. Nadal, P. J. Campagnola, J. R. Gord, and W. C. Lineberger, J. Chem. Phys. **97**, 7002 (1992).
[28] A. L. Harris, J. K. Brown, and C. B. Harris, Ann. Rev. Chem. **39**, 341 (1988).
[29] A. E. Johnson, N. E. Levinger, and P. F. Barbara, J. Phys. Chem. **96**, 7841 (1992).
[30] D. A. V. Kliner, J. C. Alfano, and P. F. Barbara, J. Chem. Phys. **98**, 5375 (1993).
[31] P. K. Walhout, J. C. Alfano, K. A. M. Thakur, and P. F. Barbara, J. Phys. Chem. **99**, 7568 (1995).
[32] U. Banin, A. Waldam, and S. Ruhman, J. Chem. Phys. **96**, 2416 (1992).
[33] I. Benjamin, U. Banion, and S. Ruhman, J. Chem. Phys. **98**, 8337 (1993).
[34] U. Banin and S. Ruhman, J. Chem. Phys. **99**, 9318 (1993).
[35] V. S. Batista and D. F. Coker, J. Chem. Phys. **106**, 6923 (1997).
[36] R. M. Bowman, M. Dantus, and A. H. Zewail, Chem. Phys. Lett. **161**, 297 (1989).
[37] N. F. Scherer, L. D. Ziegler, and G. R. Fleming, J. Chem. Phys. **96**, 5544 (1992).
[38] N. F. Scherer, D. M. Jonas, and G. R. Fleming, J. Chem. Phys. **99**, 153 (1993).
[39] Z. Li, R. Zadoyan, V. A. Apkarian, and C. C. Martens, J. Phys. Chem. **99**, 7453 (1995).
[40] R. Zadoyan, M. Sterling, and V. A. Apkarian, J. Chem. Soc. Faraday Trans. **92**, 1821 (1996).
[41] J. M. Papanikolas, P. E. Maslen, and R. Parson, J. Chem. Phys. **102**, 2452 (1995).
[42] P. E. Maslen, J. M. Papanikolas, J. Faeder, R. Parson, and S. V. Oneil, J. Phys. Chem. **96**, 7841 (1992).
[43] F. G. Amar and L. Perera, Z. Phys. D **20**, 173 (1991).
[44] L. Perera and F. G. Amar, J. Chem. Phys **90**, 7354 (1989).
[45] F. G. Amar and B. J. Berne, J. Phys. Chem. **88**, 6720 (1984).
[46] R. S. Berry, T. L. Beck, H. L. Davis, and J. Jellinek, Adv. Chem. Phys. **70**, 75 (1988).
[47] D.L. Huestis and N.E. Schlotter, J. Chem. Phys. **69**, 3100 (1969).
[48] I. Last and T. F. George, J. Chem. Phys. **87**, 1183 (1987).
[49] J. C. Tully, in *Semiempirical Methods of Electronic Structure Calculation, Part A: Techniques*, edited by G. A. Segal (Plenum, New York, 1977).
[50] E. C. M. Chen and W. E. Wentworth, J. Phys. Chem. **89**, 4099 (1985).
[51] J. A. Ayala, W. E. Wentworth, and E. C. M. Chen, J. Phys. Chem. **85**, 768 (1981).
[52] C. H. Becker, P. Casavecchia, and Y. T. Lee, J. Chem. Phys. **70**, 5477 (1979).
[53] Y. Zhao, I Yourshaw, G. Reiser, C. C. Arnold, and D. M. Neumark, J. Chem. Phys. **101**, 6538 (1994). MMSV potential contructed from equations (1),(2),(4)–(6) and parameters presented in Table VII.
[54] I. Last and T. F. George, J. Chem. Phys. **86**, 3787 (1987).
[55] I. Last and T. F. George, J. Chem. Phys. **89**, 3071 (1988).
[56] E. L. Pollock and B. J. Alder, Phys. Rev. Lett. **41**, 903 (1978).
[57] C. J. F. Bottcher, in *Theory of Electric Polarization*, edited by Z. B. Maksic (Elsevier, Amsterdam, 1952).
[58] J. Applequist, J. R. Carl, and K.-K. Fung, J. Am. Chem. Soc. **94**, 2953 (1972).
[59] V. S. Batista and D. F. Coker, J. Chem. Phys. (to be submitted).